nature geoscience

Article

https://doi.org/10.1038/s41561-022-01058-2

Martian landscapes of fluvial ridges carved from ancient sedimentary basin fill

Received: 24 July 2021

Accepted: 23 September 2022

Published online: 27 October 2022

Check for updates

Benjamin T. Cardenas [1,2], Michael P. Lamb[1] and John P. Grotzinger[1]

Large sedimentary basins contain archives of Earth history. It is unknown to what extent similar basins existed on Mars because there are few observations relating to the subsurface and it is difficult to identify buried deposits. Here, we used numerical simulations to show that landscapes of networks of topographic ridges that are abundant on the surface of Mars may represent erosional windows into thick, basin-filling river deposits that accumulated over long time spans. We used a numerical model to drive hillslope creep and differential erosion from the wind to simulate Mars-like exhumation processes acting on basin-filling fluvial strata, which we based on those buried in the Gulf of Mexico on Earth, as imaged using three-dimensional reflectance seismology. Simulations produced remarkably Martian landscapes in which the preferential erosion of mudstone relative to sandstone channel belts leads to the development of complex patterns of intersecting ridges. Our findings contrast to the existing view of ridged Martian landscapes as thin-skinned surface deposits preserving fluvial landscapes at a snapshot in time. Instead, the ridge cross-cutting patterns produced by the model reflect the exhumation of channel bodies at different stratigraphic levels, exposing basin strata accumulated over time scales of 500,000 years. Thus, we propose that fluvial ridges on Mars may expose an archive of long-lived aqueous processes.

On Earth, large sedimentary basins are a major repository for information about Earth history including sea-level change, climate change and the evolution of life[1–6]. Earth's ancient sedimentary basins importantly preserve complex organic compounds and other biosignatures as records of the early microbial biosphere and therefore provide a strong incentive for sampling on Mars[7,8]. In contrast, most basins on Mars have been located in craters with watersheds that sample relatively small parts of the ancient Martian surface[9–11], but larger depositional areas may have existed beyond craters as part of larger source-to-sink rivers influenced by broader climate conditions[12–17]. If so, the layers of sedimentary rock within those basins could contain a unique record of Martian environmental history. Part of the difficulty in identifying whether Mars had large basins is that sensors designed to image the subsurface cannot penetrate rock to great depths[18] or are stationary[19]. On Earth, large swaths of subsurface basin stratigraphy have been imaged in high-resolution three-dimensional (3D) seismic volumes, and older basin-filling rocks are exposed at the surface owing primarily to tectonic uplift and erosion. It is, however, possible that erosion on Mars, even in the absence of plate tectonic geodynamic forces to both subside and uplift basins, has also exhumed sedimentary rocks that were once deeply buried[10,12–14,16].

Networks of topographic ridges might be landforms produced during the exhumation of fluvial sedimentary rocks on Mars[12,20–24]. These ridges have the appearance of river channels in planform, but are topographic highs rather than lows (Fig. 1). One hypothesis is that fluvial ridges formed during the erosion of alluvial sequences—the

[1]Division of Geological and Planetary Sciences, California Institute of Technology, Pasadena, CA, USA. [2]Present address: Department of Geosciences, The Pennsylvania State University, University Park, PA, USA. e-mail: btcardenas@psu.edu

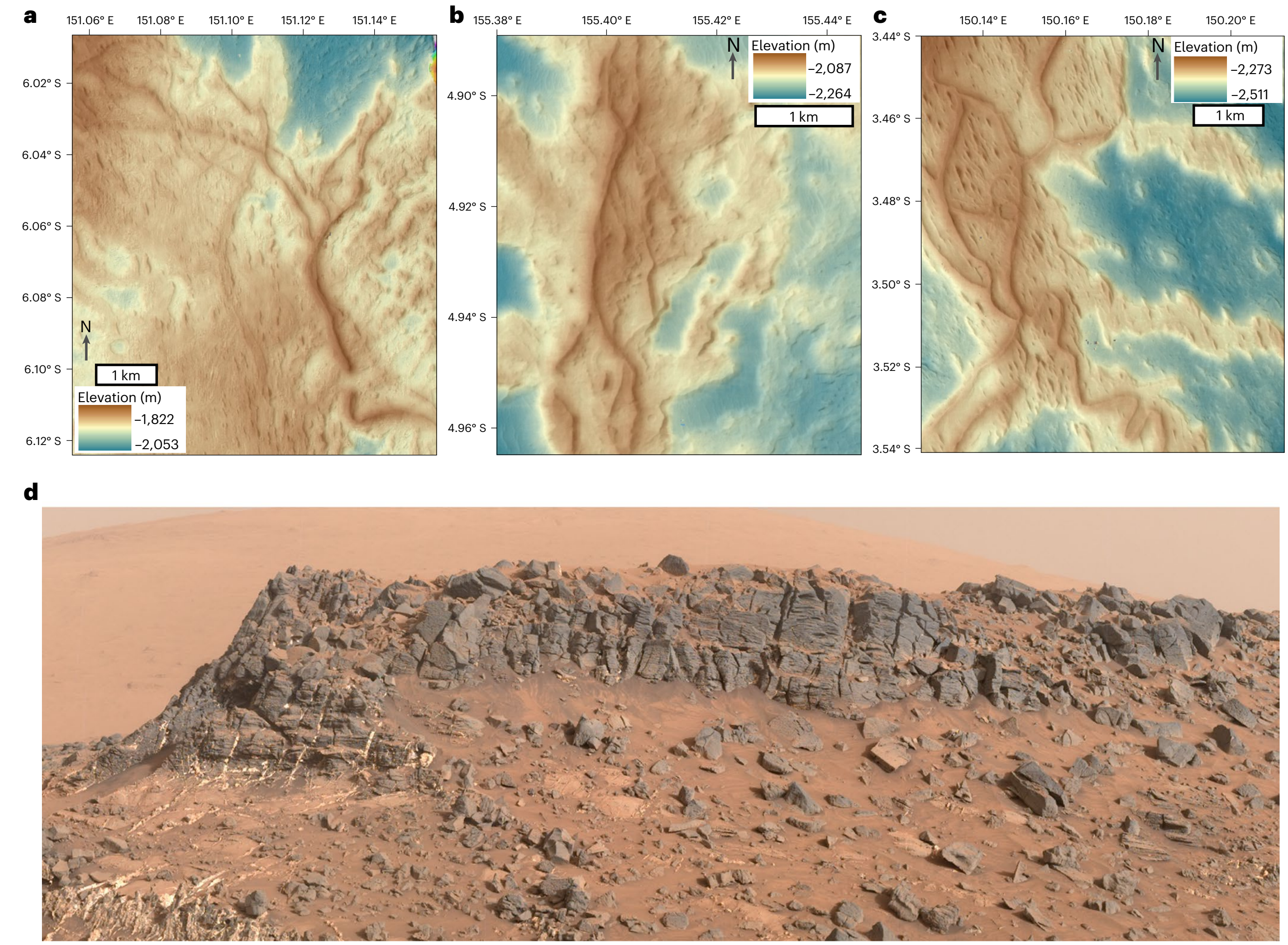

Fig. 1 | Fluvial ridges and sandstone cliffs on Mars. a–c, Digital elevation models constructed from Context Camera stereo pairs of fluvial ridges forming complex intersecting patterns exposed at Aeolis Dorsa (see Supplementary Table 2 for a list of stereo pairs): north-branching network of fluvial ridges (**a**), network of fluvial ridges branching to the north and south (**b**) and network of fluvial ridges with complex intersections (**c**). **d**, Curiosity rover Mastcam mosaic (ML_4119, sol 938) showing sandstone cliff overlying a sloping exposure of mudstones in the Murray Formation[17,25]. While this deposit is thought to be subaqueous in origin[25] rather than a fluvial ridge, it illustrates from the ground how differential erosion from the wind has led to cliff-forming sandstones that overlie slope-forming mudstones. The tip of the sandstone exposure is about 1 m thick (image credit for **a**–**d**: NASA/JPL-Caltech/MSSS).

stratigraphy accumulated within channels and along floodplains of net-depositional rivers[22]. In this scenario, fluvial ridges represent channel belts, the coarse-grained sedimentary deposits that record the lateral migration and vertical aggradation of river channels. Coarse-grained channel belts are thought to be more resistant than the finer-grained floodplain deposits surrounding channel belts, such that differential erosion by the wind or hillslope processes results in the formation of ridges[20–23], with cliff-forming sandstones often capping slope-forming mudstones[17,25,26](Fig. 1). Many fluvial ridges on Earth form in this way, representing erosional windows into thick alluvial sequences from Earth history[20,23,27–29]. Fluvial channel belts are a valuable source of information about environmental history[1], and have clear importance in reconstructing ancient aqueous environments on Mars[13,15]. Similar erosional windows into alluvial sequences on Mars would allow for high-fidelity reconstructions of the ancient Martian surface both from orbital observations and rover exploration. Another river-related ridge formation mechanism is the minor erosion of sediment lags in bypass or net-erosional rivers. Such ridges would represent a landscape at a snapshot in time rather than basin stratigraphy integrating over long time scales[29]. Other hypotheses for ridge formation exist, including subglacial eskers[30] and lava flows[31].

Exhuming basin-filling stratigraphy

Here, we tested the hypothesis that networks of topographic ridges can form from the exhumation of channel belts within thick basin-filling strata. We performed numerical landscape evolution experiments by eroding the alluvial strata of an ancient fluvial coastal plain of the Gulf of Mexico[32], now buried beneath the seafloor and imaged by 3D seismic reflectance (Fig. 2 and Extended Data Fig. 1). We used a proxy for the ratio of sandstone to mudstone[33], Ω, determined from seismic properties, which has been used previously to identify fluvial channel belts in seismic stratigraphy (Methods and Extended Data Fig. 2). We estimated the alluvial sequence imaged in the 3D seismic volume to be 136 m thick, representing over 500,000 years of deposition based on regional subsidence rates[34]. We identified 11 fluvial channel belts with high Ω surrounded by overbank strata with low Ω at different stratigraphic positions within the volume (Fig. 2). The mean channel belt thickness was 15 m with a s.d. of 8 m, while the mean width was 492 m with a s.d. of 372 m. These are comparable to the dimensions of fluvial ridge caprocks on Mars, which are on the order of 10 m thick[27] and tens to hundreds of metres wide[35].

We modelled two erosional processes thought to be important in modifying the Martian surface today and probably throughout the last

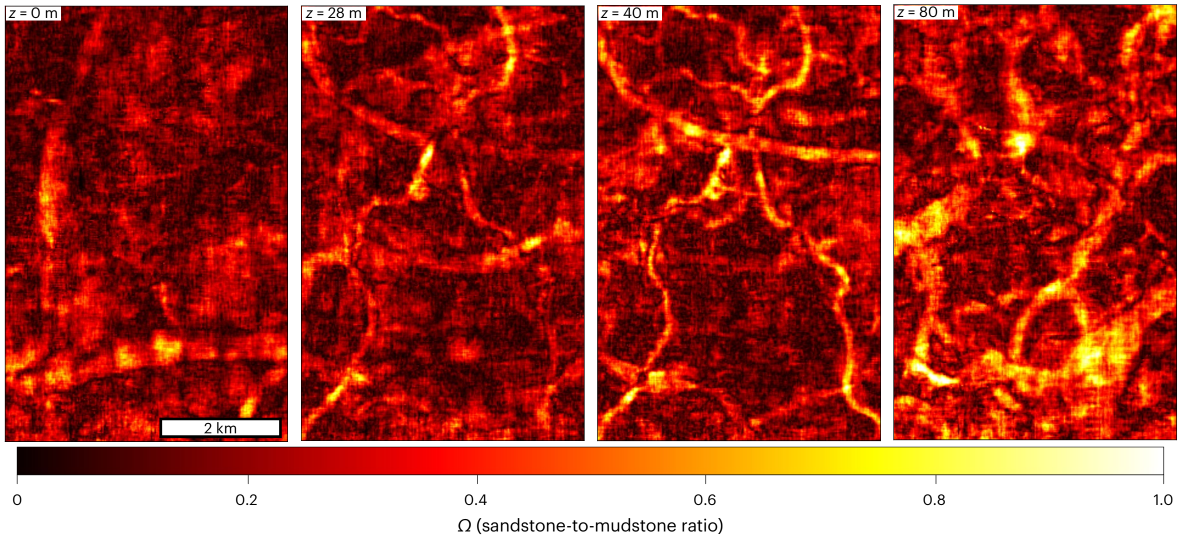

Fig. 2 | Horizontal slices showing river channel belts in the 3D seismic volume. Four horizontal slices from the 3D seismic volume. Depth, z, shows the vertical distance beneath the shallowest slice in the volume.

3 billion years: disturbance-driven hillslope soil production and creep[27], and abrasion from wind erosion[20,23] (Methods). Erosion rates by both processes were set to be a function of rock strength, and, in turn, the relative amount of stronger sandstone versus weaker mudstone as measured by Ω (Methods). There was not an imposed uplift rate at the domain boundaries, and hillslope creep is zero on a flat landscape, such that the pace of exhumation was set by wind erosion alone and soil creep acted to smooth the topography. We used the seismic volume as input into the numerical model, starting with a flat landscape. Landforms developed throughout the simulations due to differential erosion between sandstone and mudstone. We performed three numerical experiments where we varied the relative strength of wind erosion versus hillslope creep. We evolved all the landscapes over millions of years to a similar final degree of exhumation, such that the central pixel in the domain was eroded by 116 m, and compared these landscapes.

Mars-like landscapes with fluvial ridges

In experiment 1, erosion was driven 99% by the wind and 1% by hillslope soil creep (Methods). Channel belts were progressively exhumed to form sinuous topographic ridges. During exhumation, ridge evolution continued with narrowing, followed by segmentation (Fig. 3a–d and Supplementary Data Video 1). None of the ridges were completely removed in this experiment. Narrow and isolated remnants of the stratigraphically highest ridges persisted through the exhumation of the stratigraphically lowest ridges, primarily at locations where ridges were stacked vertically (Fig. 3). This experiment generated the most topographic relief (Extended Data Fig. 3). Importantly, the shape of the final landscape did not represent the pattern of channel belts or river channels at any one stratigraphic level (Fig. 2), but rather the integration of all channel belt patterns throughout the stratigraphy (Fig. 3b). This was demonstrated by the variability in ridgetop elevations, especially at locations where belts were partially stacked and topography stepped up and down from the top of one belt onto the top of another belt (Fig. 3b–f). Even along a single channel belt, erosion was variable by several metres owing to the along-belt variability in Ω observed in the seismic volume (Fig. 2).

In experiment 2 (75% driven by wind and 25% by hillslope soil creep), ridges eroded more quickly relative to the average elevation of the landscape, such that overall landscape relief was reduced (Fig. 4). The rate of soil creep scales with topographic slope. Therefore, soil creep acted to denude ridges with steep side slopes and smooth the topography. The landscape at the final time step preserved only the stratigraphically lowest channel belts as fluvial ridges, with only isolated remnants of higher channel belts preserved where they were stacked above lower channel belts (Fig. 4b and Supplementary Data Video 2). Results were similar in experiment 3 (55% driven by wind and 45% by hillslope soil creep): ridges narrowed, became segmented, and were completely removed owing to hillslope creep before stratigraphically lower channel belts were exhumed (Supplementary Data Video 3). The final landscape had low relief and lacked well-defined ridges, and thus presented no clear indicator that channel belts had been an important part of the eroded stratigraphic section (Extended Data Fig. 3 and Fig. 4). Difference maps comparing experiment 1 with the other experiments showed that patterns in erosion mimicked channel belt patterns (Fig. 4d,e).

Fluvial ridges form along erosional windows into basin stratigraphy

Experiment 1, with 99% wind-driven erosion, created a remarkably Martian landscape (Fig. 3). This synthetic landscape showed the same complexity in branching patterns and ridgetop elevations observed at Aeolis Dorsa[22,36](Fig. 1) and other regions of Mars[9,11,24,37] with fluvial ridges. Our results provide quantitative support for the hypothesis that the observed complexity in ridge patterns on Mars reflects the exhumation of channel belts from different stratigraphic levels[21–24,36,37]. Channel belts at different stratigraphic positions are best identified where ridge tops intersect at different elevations. On Mars, similar elevation offsets in crossing ridges have been observed[21,23]. Our work also is consistent with local observations from terrestrial analogues of individual ridges[23,28,29], but expands on this earlier work to show that ridge networks can be produced from deep exhumation of fluvial strata at a regional scale. Overall, our results suggest that fluvial ridges on Mars could be a surface expression of erosional windows into large, and potentially deep, ancient basins. Though some regions also show more diffuse ridges and landscapes similar to experiment 2 (for example, Arabia Terra)[12,37], the results suggest that hillslope diffusion and its driving processes, possibly including microimpacts[38], marsquakes[19] and permafrost sublimation[39], have played a lesser role than wind erosion in the exhumation of basins in Mars' dry Amazonian Period (3 billion years ago to present).

It is common on Mars to assume that ridges are thin sedimentary veneers from rivers that flowed over a landscape that was mostly

https://doi.org/10.1038/s41561-022-01058-2

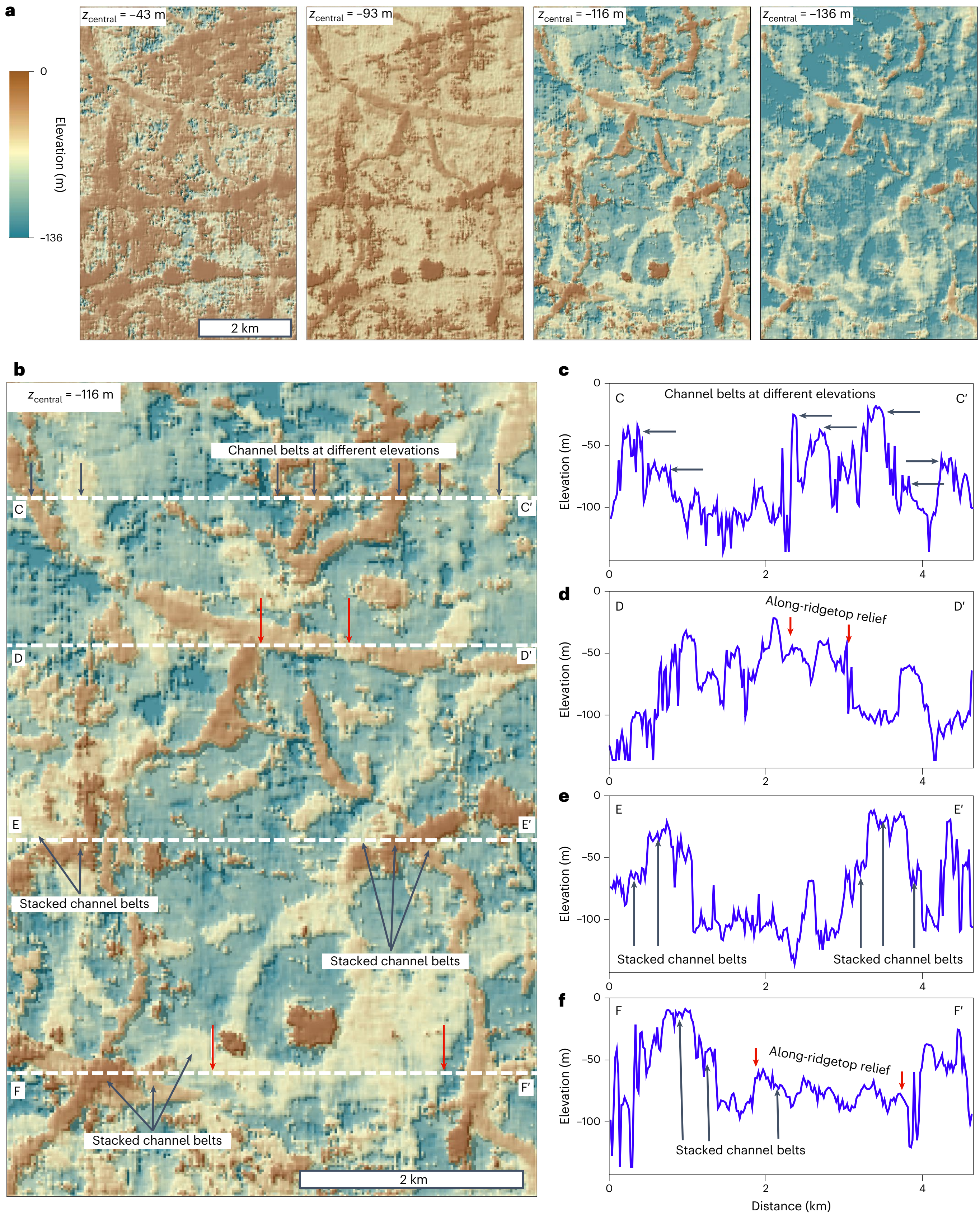

Fig. 3 | Hillshade maps showing the evolution of fluvial ridges. a, Evolution of modelled landscape topography (hillshade maps; illumination from 315° at 45°) for experiment 1 (99% wind-driven) at different erosional stages, defined by the elevation of the central pixel, $z_{central}$. **b**, Detailed results from $z_{central}$ = −58 m, showing locations of topographic profiles C–C′, D–D′, E–E′ and F–F′ as white dashed lines. Individual and stacked channel belts are annotated with grey arrows. Red arrows mark the extent of along-ridgetop profiles captured in D–D′ and F–F′. **c**–**f**, Topographic profiles C–C′ (**c**), D–D′ (**d**), E–E′ (**e**) and F–F′ (**f**) from **b** show ridge tops formed from channel belts at different stratigraphic levels and topographic breaks where channel belts are stacked. Grey arrows in **c**, **e** and **f** point to the same ridge tops as in **b**. Both **d** and **f** have 1–2 km sections along ridge tops (red arrows) where relief is variable and controlled by erosion.

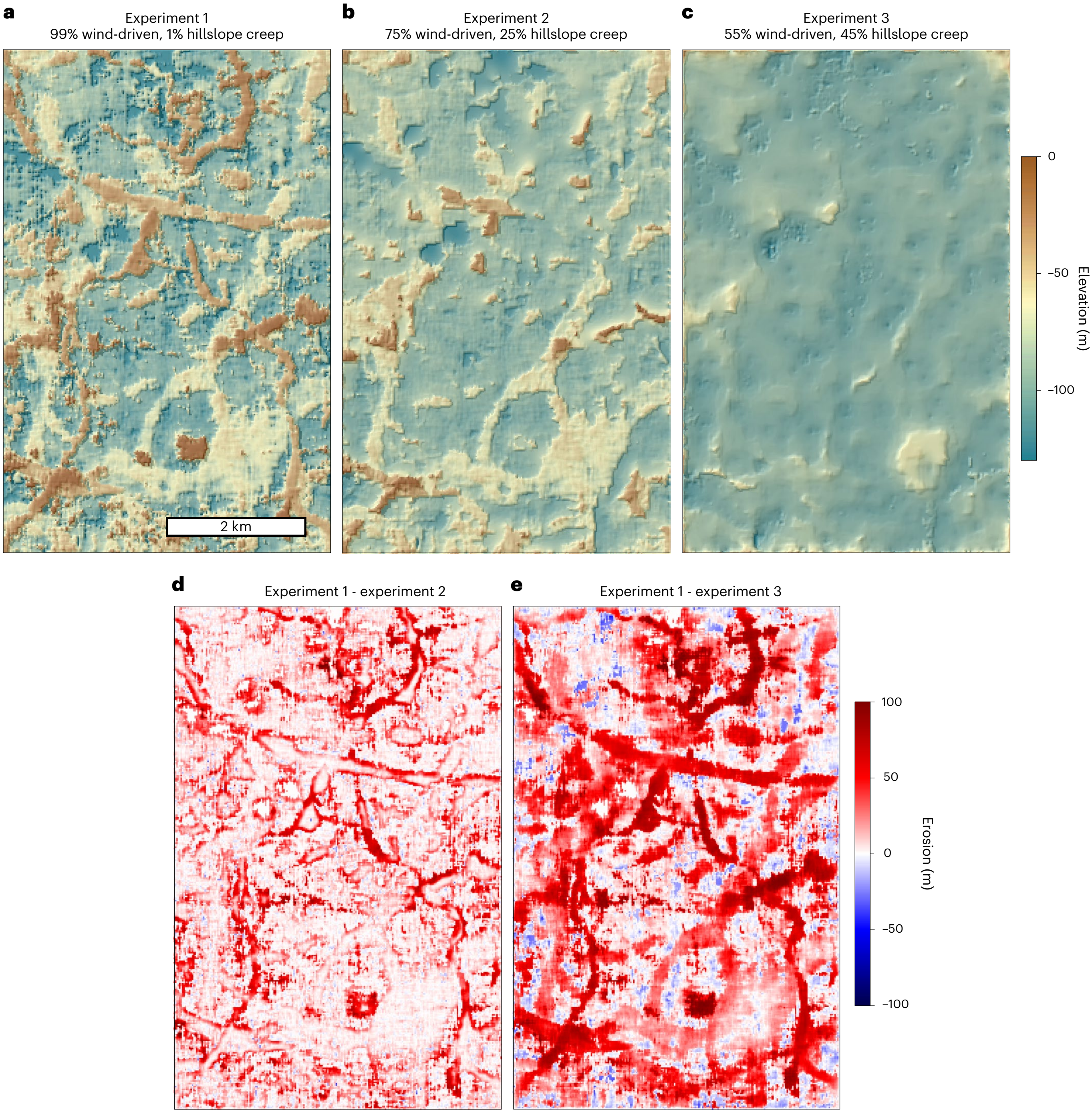

Fig. 4 | Synthetic landscapes and difference maps from the three experiments. Each landscape shown has a central cell elevation of −116 m. **a**, Experiment 1 (driven 99% by wind and 1% by hillslope creep). **b**, Experiment 2 (driven 75% by wind and 25% by hillslope creep). **c**, Experiment 3 (driven 55% by wind and 45% by hillslope creep). **d**, Map topography from experiment 1 minus experiment 2. **e**, Map topography from experiments 1 minus 3.

similar to the modern topography[35,40,41]. While there is evidence that the largest-scale topographic features on Mars, such as the topographic dichotomy and large impact basins, have persisted since Mars' river-forming era[12,42], our results showed that networks of ridges may not represent an inverted ancient riverine landscape. Instead, the modern landscape of ridges reflects differential erosion into basin stratigraphy accumulated over long time scales in which deposits of different ages and different stratigraphic levels are now exposed at the land surface. The high-relief landscapes we generated in our experiments are in great contrast to the relatively flat relief of the coastal plain setting in which the stratigraphy originally accumulated[32], without needing to invoke tectonic tilting or warping to explain complexity in relief[40]. Reconstructing ancient environments from fluvial stratigraphy challenges a common assumption in planetary surface processes. Instead of relying on modern regional topography to guide interpretations of river network patterns and channel slopes, the ridges, instead, may be a topographic indicator of an erosional window into ancient worlds encoded into stratigraphy[12].

The evidence that ridges represent exposed stratigraphy of several channelized deposits may also support a fluvial origin over other hypotheses. For example, although eskers are depositional landforms, they form beneath glaciers in what is typically a net-erosional environment[43], which precludes the preservation of thick sequences of stacked, channelized deposits. Preserved eskers in the ancient rock record are rare on Earth, and where they occur, they require special circumstances, such as deglaciation and sea-level rise to shift to a net-depositional environment[44]. Even in that case[44], the deposit is only from a single esker, not a sequence of channelized deposits at different stratigraphic levels. Likewise, lava flows that generate ridges form from lava filling a single river valley, typically in a net/erosional landscape[29], and therefore would also lack the stratigraphic architecture of ridges on Mars. In broader lava fields, flows can self-channelize like rivers and form multiple branches and lobes[45]. However, unlike rivers that sort sand and mud between channel and floodplain deposits, lava fields lack a similar mechanism to create systematic spatial variations in rock strength, which are necessary for ridge formation during exhumation[20,23].

The Martian stratigraphic record

On Earth, the sedimentary record is built within basins, where sediment accumulation is accommodated by relatively slow subsidence driven by a number of possible processes[3], including tectonics. These types of basins may not have existed on early Mars, as a lack of plate tectonics and a thick, rigid lithosphere would not have supported slow subsidence[13]. Accommodation space for long-lasting deposition on ancient Mars may instead have been created instantaneously during impacts, including the creation of the hemispheric topographic dichotomy[46]. Rapidly generated accommodation space on Earth allows for the unusually complete preservation of sedimentary deposits[47], rather than the more typical deposit reworking and signal degradation[48,49]. That is, not only might the sedimentary record of Mars be well exposed along erosional windows, but the exposed stratigraphy may be an exceptionally complete record of Martian history during the planet's most habitable period. Notably, the intracrater plains of the southern hemisphere also have networks of fluvial ridges downstream of erosional valley networks, indicating the potential for long-lived source-to-sink river systems terminating in basins much larger than craters[12]. Fluvial strata exposed in erosional windows are the guide to finding favourable preservation of organic compounds and other potential biosignatures[7,8].

Online content

Any methods, additional references, Nature Research reporting summaries, source data, extended data, supplementary information, acknowledgements, peer review information; details of author contributions and competing interests; and statements of data and code availability are available at https://doi.org/10.1038/s41561-022-01058-2.

References

1. Foreman, B. Z., Heller, P. L. & Clementz, M. T. Fluvial response to abrupt global warming at the Palaeocene/Eocene boundary. *Nature* **491**, 92–95 (2012).
2. Paola, C. Quantitative models of sedimentary basin filling. *Sedimentology* **47**, 121–178 (2000).
3. Nyberg, B. & Howell, J. A. Is the present the key to the past? A global characterization of modern sedimentary basins. *Geology* **43**, 643–646 (2015).
4. McMahon, W. J. & Davies, N. S. Evolution of alluvial mudrock forced by early land plants. *Science* **359**, 1022–1024 (2018).
5. Simms, A. R., Anderson, J. B., Milliken, K. T., Taha, Z. P. & Wellner, J. S. Geomorphology and age of the oxygen isotope stage 2 (last lowstand) sequence boundary on the northwestern Gulf of Mexico continental shelf. *Geol. Soc. Lond. Spec. Publ.* **277**, 29–46 (2007).
6. Cloud, P. Paleoecological significance of the banded iron-formation. *Econ. Geol.* **68**, 1135–1143 (1973).
7. Summons, R. E. et al. Preservation of Martian organic and environmental records: final report of the Mars Biosignature Working Group. *Astrobiology* **11**, 157–181 (2011).
8. McMahon, S. et al. A field guide to finding fossils on Mars. *J. Geophys. Res. Planets* **123**, 1012–1040 (2018).
9. Goudge, T. A., Mohrig, D., Cardenas, B. T., Hughes, C. M. & Fassett, C. I. Stratigraphy and paleohydrology of delta channel deposits, Jezero Crater, Mars. *Icarus* **301**, 58–75 (2018).
10. Grotzinger, J. P. et al. Deposition, exhumation, and paleoclimate of an ancient lake deposit, Gale Crater, Mars. *Science* **350**, aac7575–aac7575 (2015).
11. Irwin, R. P., Lewis, K. W., Howard, A. D. & Grant, J. A. Paleohydrology of Eberswalde Crater, Mars. *Geomorphology* **240**, 83–101 (2015).
12. Dickson, J. L., Lamb, M. P., Williams, R. M. E., Hayden, A. T. & Fischer, W. W. The global distribution of depositional rivers on early Mars. *Geology* **49**, 504–509 (2020).
13. Grotzinger, J. P. & Milliken, R. E. Sedimentary geology of Mars. *Society for Sedimentary Geology* https://doi.org/10.2110/pec.12.102 (2012).
14. Malin, M. C. & Edgett, K. S. Mars Global Surveyor Mars Orbiter Camera: interplanetary cruise through primary mission. *J. Geophys. Res.* **106**, 23429–23570 (2001).
15. Malin, M. C. & Edgett, K. S. Evidence for persistent flow and aqueous sedimentation on early Mars. *Science* **302**, 1931–1934 (2003).
16. Edgett, K. S. et al. Extraformational sediment recycling on Mars. *Geosphere* https://doi.org/10.1130/GES02244.1 (2020).
17. Edgett, K. S. & Sarkar, R. Recognition of sedimentary rock occurrences in satellite and aerial images of other worlds—insights from Mars. *Remote Sens.* **13**, 4296 (2021).
18. Carter, L. M. et al. Shallow radar (SHARAD) sounding observations of the Medusae Fossae Formation, Mars. *Icarus* **199**, 295–302 (2009).
19. Banerdt, W. B. et al. Initial results from the InSight mission on Mars. *Nat. Geosci.* **13**, 183–189 (2020).
20. Williams, R. M. E., Jr, Thomas, C. C. & Eby, D. E. Exhumed paleochannels in central Utah—analogs for raised curvilinear features on Mars. in *Central Utah: Diverse Geology of a Dynamic Landscape* 221–235 (Utah Geological Association, 2007).
21. Cardenas, B. T., Mohrig, D. & Goudge, T. A. Fluvial stratigraphy of valley fills at Aeolis Dorsa, Mars: evidence for base-level fluctuations controlled by a downstream water body. *GSA Bull.* **130**, 484–498 (2018).
22. DiBiase, R. A., Limaye, A. B., Scheingross, J. S., Fischer, W. W. & Lamb, M. P. Deltaic deposits at Aeolis Dorsa: sedimentary evidence for a standing body of water on the northern plains of Mars. *J. Geophys. Res. Planets* **118**, 1285–1302 (2013).
23. Hayden, A. T. et al. Formation of sinuous ridges by inversion of river-channel belts in Utah, USA, with implications for Mars. *Icarus* **332**, 92–110 (2019).
24. Balme, M. R. et al. Aram Dorsum: an extensive mid-Noachian age fluvial depositional system in Arabia Terra, Mars. *J. Geophys. Res. Planets* **125**, e2019JE006244 (2020).
25. Stack, K. M. et al. Evidence for plunging river plume deposits in the Pahrump Hills member of the Murray Formation, Gale Crater, Mars. *Sedimentology* **66**, 1768–1802 (2019).
26. Day, M. & Kocurek, G. Observations of an aeolian landscape: from surface to orbit in Gale Crater. *Icarus* **280**, 37–71 (2016).
27. Hayden, A. T. & Lamb, M. P. Fluvial sinuous ridges of the Morrison Formation, USA: meandering, scarp retreat, and implications for mars. *J. Geophys. Res. Planets* **125**, e2020JE006470 (2020).

28. Cardenas, B. T. et al. The anatomy of exhumed river-channel belts: bedform to belt-scale river kinematics of the Ruby Ranch Member, Cretaceous Cedar Mountain Formation, Utah, USA. *Sedimentology* **67**, 3655–3682 (2020).
29. Zaki, A. S., Pain, C. F., Edgett, K. S. & Castelltort, S. Global inventory of fluvial ridges on Earth and lessons applicable to Mars. *Earth Sci. Rev.* **216**, 103561 (2021).
30. Butcher, F. E. G., Conway, S. J. & Arnold, N. S. Are the Dorsa Argentea on Mars eskers? *Icarus* **275**, 65–84 (2016).
31. Bleacher, J. E. et al. Plateaus and sinuous ridges as the fingerprints of lava flow inflation in the Eastern Tharsis Plains of Mars. *J. Volcanol. Geotherm. Res.* **342**, 29–46 (2017).
32. Milliken, K. T., Blum, M. D., Snedden, J. W. & Galloway, W. E. Application of fluvial scaling relationships to reconstruct drainage-basin evolution and sediment routing for the Cretaceous and Paleocene of the Gulf of Mexico. *Geosphere* **14**, 749–767 (2018).
33. Hart, B. S. Channel detection in 3-D seismic data using sweetness. *American Association of Petroleum Geologists Bulletin* **92**, 733–742 (2008).
34. Straub, K. M., Paola, C., Mohrig, D., Wolinsky, M. A. & George, T. Compensational stacking of channelized sedimentary deposits. *J. Sediment. Res.* **79**, 673–688 (2009).
35. Kite, E. S. et al. Persistence of intense, climate-driven runoff late in Mars history. *Sci. Adv.* **5**, eaav7710 (2019).
36. Hughes, C. M., Cardenas, B. T., Goudge, T. A. & Mohrig, D. Deltaic deposits indicative of a paleo-coastline at Aeolis Dorsa, Mars. *Icarus* **317**, 442–453 (2019).
37. Davis, J. M. et al. A diverse array of fluvial depositional systems in Arabia Terra: evidence for mid-Noachian to early Hesperian rivers on Mars. *J. Geophys. Res. Planets* **124**, 1913–1934 (2019).
38. Howard, A. D. Simulating the development of Martian highland landscapes through the interaction of impact cratering, fluvial erosion, and variable hydrologic forcing. *Geomorphology* **91**, 332–363 (2007).
39. Aylward, D. S., Schmidt, L. M. & Levy, J. S. Formation of coarse sediment lags in ice–sediment mixtures: a geomorphic signature of sublimation on regolith surfaces. *Planet. Space Sci.* **174**, 8–13 (2019).
40. Lefort, A., Burr, D. M., Beyer, R. A. & Howard, A. D. Inverted fluvial features in the Aeolis-Zephyria Plana, western Medusae Fossae Formation, Mars: evidence for post-formation modification. *J. Geophys. Res. Planets* **117**, E03007 (2012).
41. Matsubara, Y. et al. River meandering on Earth and Mars: a comparative study of Aeolis Dorsa meanders, Mars and possible terrestrial analogs of the Usuktuk River, AK, and the Quinn River, NV. *Geomorphology* **240**, 102–120 (2015).
42. Irwin, R. P. & Watters, T. R. Geology of the Martian crustal dichotomy boundary: age, modifications, and implications for modeling efforts. *J. Geophys. Res. Planets* **115**, E11006 (2010).
43. Brennand, T. A. Macroforms, large bedforms and rhythmic sedimentary sequences in subglacial eskers, south-central Ontario: implications for esker genesis and meltwater regime. *Sediment. Geol.* **91**, 9–55 (1994).
44. Cummings, D. I. et al. Sequence stratigraphy of a glaciated basin fill, with a focus on esker sedimentation. *GSA Bull.* **123**, 1478–1496 (2011).
45. Rhéty, M. et al. A comparison of cooling-limited and volume-limited flow systems: examples from channels in the Piton de la Fournaise April 2007 lava-flow field. *Geochem. Geophys. Geosyst.* **18**, 3270–3291 (2017).
46. Andrews-Hanna, J. C., Zuber, M. T. & Banerdt, W. B. The Borealis Basin and the origin of the Martian crustal dichotomy. *Nature* **453**, 1212–1215 (2008).
47. Ganti, V., Hajek, E. A., Leary, K., Straub, K. M. & Paola, C. Morphodynamic hierarchy and the fabric of the sedimentary record. *Geophys. Res. Lett.* **47**, e2020GL087921 (2020).
48. Jerolmack, D. J. & Paola, C. Shredding of environmental signals by sediment transport. *Geophys. Res. Lett.* **37**, L19401 (2010).
49. Paola, C., Ganti, V., Mohrig, D., Runkel, A. C. & Straub, K. M. Time not our time: physical controls on the preservation and measurement of geologic time. *Annu. Rev. Earth Planet. Sci.* **46**, 409–438 (2018).

Methods

Three-dimensional seismic volume

Cenozoic-aged strata buried in the subsurface Gulf of Mexico accumulated in a variety of near-coastal environments, including delta topsets, coastal plains, incised valleys and submarine environments, with variability driven by sea-level change and the reorganization of drainage basins and sediment routing across North America[32,50–54]. We acquired 3D seismic volume B-11-92-LA from the U.S. Geological Survey's National Archive of Marine Seismic Surveys website (https://walrus.wr.usgs.gov/NAMSS/; Extended Data Fig. 1), in which we identified fluvial channel belts in every horizontal slice in the time interval of 484–620 ms of two-way travel time (ms TWT, a proxy for depth; Fig. 2). These features were interpreted as fluvial channel belts rather than submarine channel belts or fault windows on the basis of their elongated planview geometry and width-to-thickness ratios greater than 1 (ref. [55]). We defined a smaller subset of the survey at this time interval bound by crosslines 402–1,521 and inlines 1,900–2,822 to decrease the processing time. The study area was ~4 km × 7 km with 20 m pixel resolution (Extended Data Fig. 1). We assumed that 1 ms TWT is equivalent to 1 m depth[34], producing a voxel thickness of 4 m and a total stratigraphic thickness of 136 m based on the 4 ms sampling rate reported in the volume metadata. We assumed the same conversion to depth as used for the entire volume, though this conversion is only an estimate and is likely to be spatially variable. Assuming a subsidence rate of 0.26 m kyr^{-1} (ref. [34]), we calculated this stratigraphic package to have accumulated over the course of ~500,000 years.

In Petrel, we converted the original amplitude volume into a sweetness volume. Sweetness is a seismic attribute equal to the instantaneous amplitude divided by the square root of the instantaneous frequency[56]. Sweetness reflects the ratio of sandstone to mudstone, and is exceedingly useful for identifying fluvial channel belts[33,57–59]. The contrasting lithologies of alluvial stratigraphy, where channel belts are more sandstone rich and overbank strata are more mudstone rich, is thought to be the primary mechanism creating the spatially variable erosion rates that lead to fluvial ridge formation[20,23,27], and thus sweetness is the lithology attribute we used to set the rates of landscape evolution processes in the model. Channel belt thicknesses were measured in milliseconds of TWT every ten crosslines directly in Petrel using the measure tool ($n = 84$). Channel belt widths were measured by mapping channel belt edges using scaled horizontal slices in ArcGIS, and calculating the distance from each point on one edge of the belt to the closest point on the opposite edge. We report a mean width for every belt ($n = 11$), and the s.d. of the means.

Using the Python program 'segyio' (https://github.com/equinor/segyio), we converted the volume to a 3D numpy array for further processing. Raw sweetness values were well described by a gamma distribution (Extended Data Fig. 2). For normalization purposes, we defined Ω as a dimensionless number equal to the sweetness value divided by the maximum sweetness; thus, Ω varies from 0 to 1, with a mean of 0.30 and a s.d. of 0.18.

Landscape evolution sensitive to lithology

We imported the sweetness volume into a landscape evolution model we built using a Landlab grid with open boundaries[60,61]. We set the resolution of the grid to 20 m, the lateral resolution of the seismic volume. This is similar to the 18 m resolution of Context Camera stereo-pair digital elevation models of the Martian surface[62,63] (Fig. 1a–c). The model simulated two processes that evolved topography through erosion based on sweetness sampled from the seismic volume and topographic slope. The first process was wind-driven sand abrasion, which is common on modern Mars and known to produce lithology-sensitive erosion rates[20,23,28,64–66]. We modelled this process using a spatially variable erosion rate that depended on Ω in each cell sampled from the seismic volume. The second process was disturbance-driven soil creep (for example, due to microimpacts[38], marsquakes[19] and permafrost[39]), which we modelled using linear topographic diffusion. The governing equation was

$$\frac{\mathrm{d}z}{\mathrm{d}t} = -(E_\mathrm{a} + E_\mathrm{d}), \qquad (1)$$

where z is the positive-upward vertical dimension, t is time, $-\frac{\mathrm{d}z}{\mathrm{d}t}$ is the total vertical erosion rate resulting from wind-driven (aeolian) erosion, E_a, and topographic diffusion, E_d.

Aeolian sand transport is largely driven by grain-on-grain impacts during saltation[67]. Impacts from saltating grains are an important component of aeolian sediment transport[67], and the abrasion of rock by saltating sand grains is an important erosional process on Mars[26,64,68]. Given that fluvial ridge formation requires erosion to be sensitive to lithology[20,23], and that there is no agreed-on erosion law for modelling landscape-scale wind-driven exhumation over long time scales[68,69], we took a simple approach. We defined E_a as

$$E_\mathrm{a} = \frac{K_1}{\Omega^m}, \qquad (2)$$

where we set $m = 2$ because erosion rate scales inversely squared with tensile strength for abrasion processes driven by repetitive impacts[70], under the assumption that tensile strength, in turn, might be proportional to sweetness. K_1 is a rate constant (with dimensions of L/T).

The second term of equation (1) describes topographic change associated with soil creep, which is modelled using linear topographic diffusion as[38]

$$E_\mathrm{d} = -K_2 \nabla^2 z, \qquad (3)$$

where K_2 is soil diffusivity with dimensions of L^2/T, and $\nabla^2 z$ is the local topographic curvature with dimensions of 1/L. We set K_2 to vary with Ω, on the basis of the observation that sandstones tend to form vertical cliffs whereas mudstones tend to form hillslopes[23,27] (Fig. 1):

$$K_2 = \frac{K_3}{\Omega^n}. \qquad (4)$$

In all experiments, we set n equal to 1. K_3 has dimensions of L^2/T.

We performed three experiments where we explored landscapes produced by relative amounts of wind-driven erosion and diffusion. The rates of surface erosion on Mars have been estimated by various means to range from 10^{-5} m Myr^{-1} to 1 m Myr^{-1} (refs. [71,72]), but are mostly unknown. Here, we set K_1 to 1 m Myr^{-1}, but since we analysed the results only in the space of the landforms created, the results are insensitive to absolute rates. Time steps vary between and within experiments, but on the basis of our selected range of diffusivities and the number of turns, we estimate our results to represent millions of years of erosion. To explore the impact of hillslope creep, we varied K_3 from 0.01 to 100 m^2 Myr^{-1}, a range reasonable for values measured on Earth[73]. In experiments 1, 2 and 3, we set $K_3 = 0.01$, 2 and 100 m^2 Myr^{-1}, respectively.

Each experiment started with a flat surface at the top of the seismic volume. At each time step, equation (1) was solved, the topographic surface was updated and the Ω of the surface was updated to reflect the intersection of topography with stratigraphy. We specifically tracked the elevation of the central pixel of the landscape, as we compared landscapes produced from different experiments when they shared the same central pixel value (Fig. 4). We calculated the total topographic change by each process as the sum of the absolute value of elevation change multiplied by cell area. If the maximum erosion during any time step was greater than 4 m (that is, the estimated vertical resolution of the seismic volume), the time step was reduced.

Data availability

The 3D seismic volume used to generate the experimental results is available in Caltech's Research Data Repository[74].

Code availability

The numerical model used in the experiments is available in Caltech's Research Data Repository[74].

References

50. Galloway, W. E., Whiteaker, T. L. & Ganey-Curry, P. History of Cenozoic North American drainage basin evolution, sediment yield, and accumulation in the Gulf of Mexico basin. *Geosphere* **7**, 938–973 (2011).
51. Galloway, W. E., Ganey-Curry, P. E., Li, X. & Buffler, R. T. Cenozoic depositional history of the Gulf of Mexico basin. *AAPG Bull.* **84**, 1743–1774 (2000).
52. Blum, M. & Pecha, M. Mid-Cretaceous to Paleocene North American drainage reorganization from detrital zircons. *Geology* **42**, 607–610 (2014).
53. Wood, L. J. Quantitative seismic geomorphology of Pliocene and Miocene fluvial systems in the Northern Gulf of Mexico, U.S.A. *J. Sediment. Res.* **77**, 713–730 (2007).
54. Maynard, J. R. Fluvial response to active extension: evidence from 3D seismic data from the Frio Formation (Oligo–Miocene) of the Texas Gulf of Mexico Coast, USA. *Sedimentology* **53**, 515–536 (2006).
55. Jobe, Z. R., Howes, N. C. & Auchter, N. C. Comparing submarine and fluvial channel kinematics: implications for stratigraphic architecture. *Geology* **44**, 931–934 (2016).
56. Radovich, B. J. & Oliveros, R. B. 3-D sequence interpretation of seismic instantaneous attributes from the Gorgon Field. *Lead. Edge* **17**, 1286–1293 (1998).
57. Hart, B. Stratigraphically significant attributes. *Lead. Edge* **27**, 320–324 (2008).
58. Hart, B. S. Whither seismic stratigraphy? *Interpretation* **1**, SA3–SA20 (2013).
59. Armstrong, C., Mohrig, D., Hess, T., George, T. & Straub, K. M. Influence of growth faults on coastal fluvial systems: examples from the late Miocene to Recent Mississippi River Delta. *Sediment. Geol.* **301**, 120–132 (2014).
60. Hobley, D. E. J. et al. Creative computing with Landlab: an open-source toolkit for building, coupling, and exploring two-dimensional numerical models of Earth-surface dynamics. *Earth Surf. Dynam.* **5**, 21–46 (2017).
61. Barnhart, K. R. et al. Short communication: Landlab v2.0: a software package for Earth surface dynamics. *Earth Surf. Dynam.* **8**, 379–397 (2020).
62. Beyer, R. A., Alexandrov, O. & McMichael, S. The Ames Stereo Pipeline: NASA's open source software for deriving and processing terrain data. *Earth Space Sci.* **5**, 537–548 (2018).
63. Malin, M. C. et al. Context Camera investigation on board the Mars Reconnaissance Orbiter. *J. Geophys. Res. Planets* **112**, E05S04 (2007).
64. Sagan, C. Sandstorms and eolian erosion on Mars. *J. Geophys. Res. (1896–1977)* **78**, 4155–4161 (1973).
65. Pain, C. F., Clarke, J. D. A. & Thomas, M. Inversion of relief on Mars. *Icarus* **190**, 478–491 (2007).
66. Burr, D. M. et al. Pervasive aqueous paleoflow features in the Aeolis/Zephyria Plana region, Mars. *Icarus* **200**, 52–76 (2009).
67. Anderson, R. S. & Haff, P. K. Simulation of eolian saltation. *Science* **241**, 820–823 (1988).
68. Day, M., Anderson, W., Kocurek, G. & Mohrig, D. Carving intracrater layered deposits with wind on Mars. *Geophys. Res. Lett.* **43**, 2473–2479 (2016).
69. Kite, E. S., Lewis, K. W., Lamb, M. P., Newman, C. E. & Richardson, M. I. Growth and form of the mound in Gale Crater, Mars: slope wind enhanced erosion and transport. *Geology* **41**, 543–546 (2013).
70. Sklar, L. S. & Dietrich, W. E. Sediment and rock strength controls on river incision into bedrock. *Geology* **29**, 1087–1090 (2001).
71. Golombek, M. P. et al. Small crater modification on Meridiani Planum and implications for erosion rates and climate change on Mars. *J. Geophys. Res. Planets* **119**, 2522–2547 (2014).
72. Golombek, M. P. et al. Erosion rates at the Mars Exploration Rover landing sites and long-term climate change on Mars. *J. Geophys. Res.* **111**, E12S10 (2006).
73. Richardson, P. W., Perron, J. T. & Schurr, N. D. Influences of climate and life on hillslope sediment transport. *Geology* **47**, 423–426 (2019).
74. Cardenas, B.T. Martian landscapes carved from ancient sedimentary basin fill – data and model [data set]. *CaltechDATA* https://doi.org/10.22002/D1.20023 (2022).

Acknowledgements

Funding for this study was provided in part by NASA grant NNX16AQ81G awarded to M.P.L. We thank the Mars Science Laboratory mission for support and J. Dickson for technical assistance in Caltech's Murray Lab for Planetary Visualization.

Author contributions

B.T.C. and M.P.L. conceived the work and applied the methodology. All authors contributed to the analysis, writing, reviewing and editing.

Competing interests

The authors declare no competing interests.

Additional information

Extended data is available for this paper at https://doi.org/10.1038/s41561-022-01058-2.

Supplementary information The online version contains supplementary material available at https://doi.org/10.1038/s41561-022-01058-2.

Correspondence and requests for materials should be addressed to Benjamin T. Cardenas.

Peer review information *Nature Geoscience* thanks Joel Davis and Nicolas Mangold for their contribution to the peer review of this work. Primary Handling Editors: Tamara Goldin and James Super, in collaboration with the *Nature Geoscience* team.

 https://doi.org/10.1038/s41561-022-01058-2

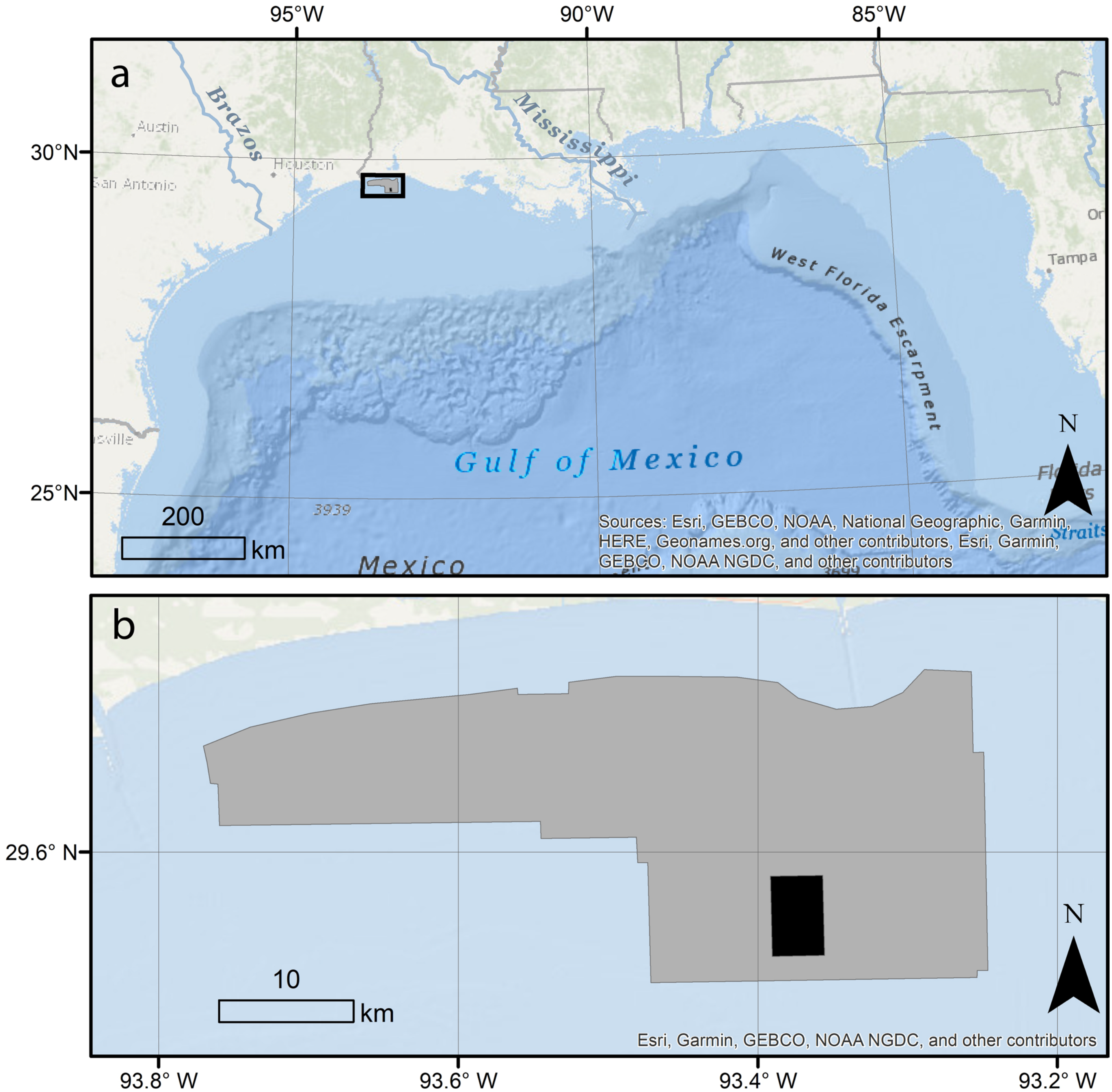

Extended Data Fig. 1 | Location maps of the seismic volume used in the experiment. A: Box shows the location of seismic volume B-11-91-LA relative to the Gulf of Mexico, Earth. B: Zoom in to the box in A, showing the full extent of the 3D seismic survey (gray area) and the subsection used in the experiments (black area).

https://doi.org/10.1038/s41561-022-01058-2

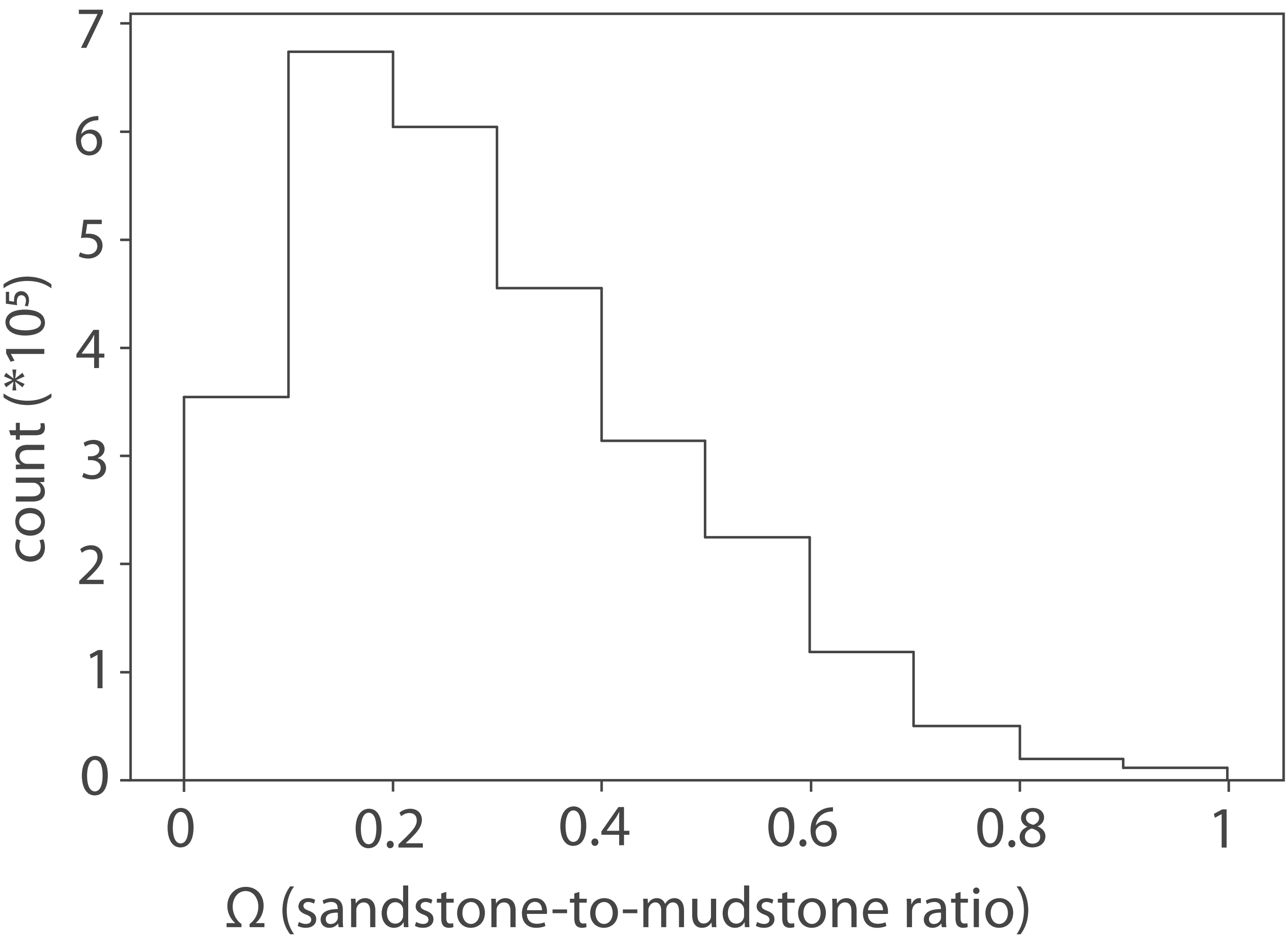

Extended Data Fig. 2 | The distribution of Ω. Histogram showing the distribution of the dimensionless sweetness of the full seismic volume.

https://doi.org/10.1038/s41561-022-01058-2

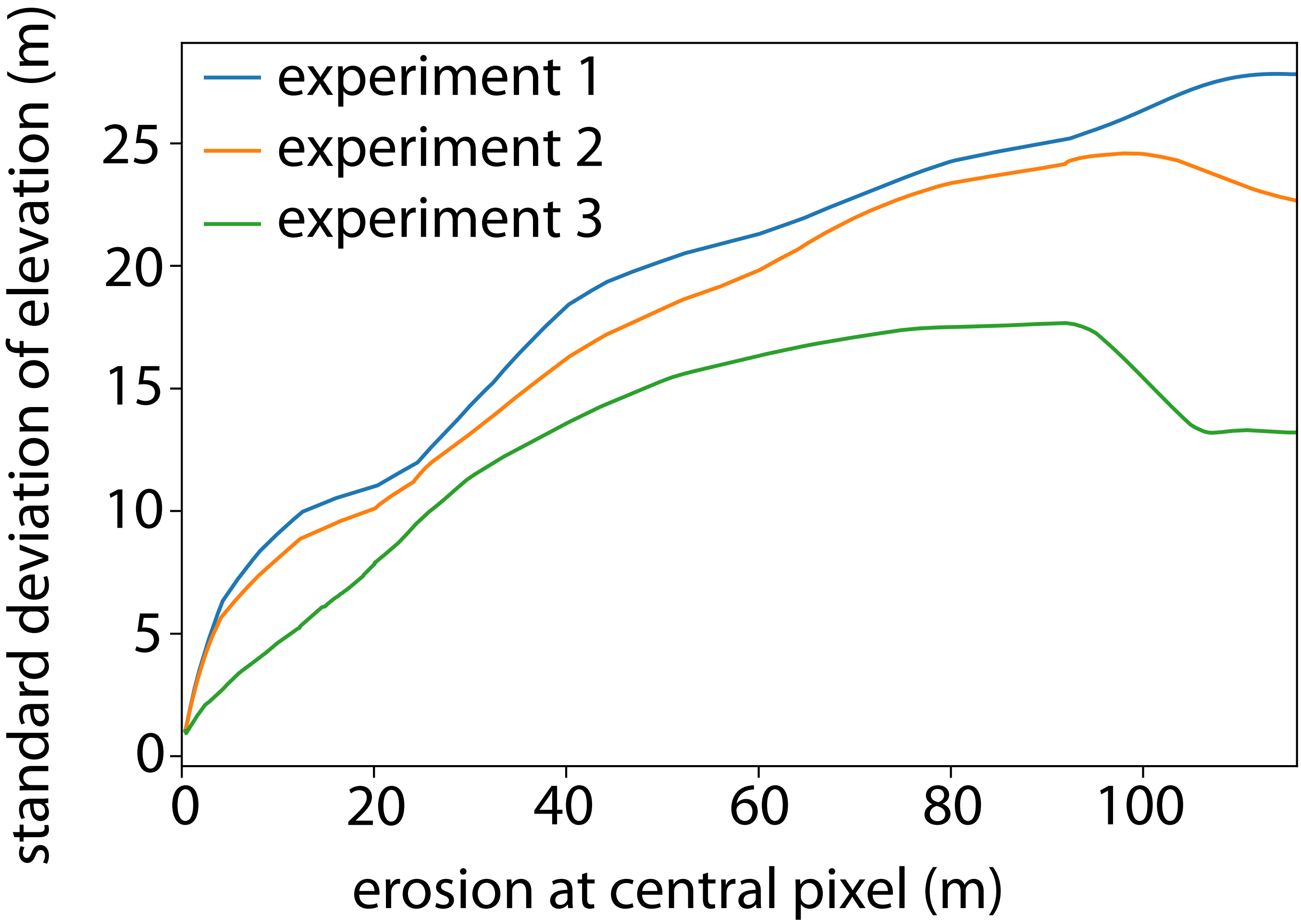

Extended Data Fig. 3 | Evolution of topographic relief in each experiment relative to the erosion at the central pixel. The standard deviation of elevation generated during experiments 1 (99% wind-driven, 1% hillslope creep), 2 (75% wind-driven, 25% hillslope creep), and 3 (55% wind-driven, 45% hillslope creep). The experiments with less topographic variability evolved fewer fluvial ridges. Comparisons in Fig. 4 were performed when all experiments eroded the central pixel by 116 m, the value at the end of this plot.